Scientific Research Publishing

World Journal of Nuclear Science and Technology, 2026, 16(4), 121-133
https://www.scirp.org/journal/wjnst
ISSN Online: 2161-6809
ISSN Print: 2161-6795

CFD-Based Optimization of UT Inspection Grid Spacing for Detecting Cavitation Erosion in Piping Components

Kyeongmo Hwang, Bongjin Ko, Jonghyeon Kim, Junhyeon Park

Safety Evaluation Group, Standard Testing & Engineering Company, Daejeon, Korea
Email: hkm@stdte.co.kr

How to cite this paper: Hwang, K., Ko, B., Kim, J. and Park, J. (2026) CFD-Based Optimization of UT Inspection Grid Spacing for Detecting Cavitation Erosion in Piping Components. *World Journal of Nuclear Science and Technology*, **16**, 121-133.
https://doi.org/10.4236/wjnst.2026.164008

Received: October 10, 2026
Accepted: October 28, 2026
Published: October 31, 2026

Copyright © 2026 by author(s) and Scientific Research Publishing Inc.
This work is licensed under the Creative Commons Attribution International License (CC BY 4.0).
http://creativecommons.org/licenses/by/4.0/

Open Access

Abstract

Representative aging mechanisms responsible for erosion in piping systems installed in nuclear power plants include cavitation, flashing, liquid droplet impingement erosion, and solid particle erosion. Unlike general corrosion and flow-accelerated corrosion (FAC), which typically affect relatively large areas, these erosion mechanisms can cause highly localized damage. Because erosion results in localized wall thinning, the ultrasonic testing (UT), which is widely used for pipe wall thickness inspection, may have limitations in accurately identifying localized damage. Accordingly, this study investigated the flow variables associated with erosion-prone regions using computational fluid dynamics (CFD) and determined an appropriate UT inspection grid spacing based on the axial distance over which these variables influence the inner pipe wall. The commercial CFD code ANSYS FLUENT was employed for all simulations. Cavitation analyses were performed for four pipe sizes equipped with an orifice plate by varying the inlet pressure under five or six operating conditions for each pipe size. To determine an appropriate inspection grid spacing for detecting erosion damage, the UT grid spacings specified in EPRI NSAC-202L were used as a reference for comparison.

Keywords

Cavitation, UT Inspection, UT Grid Spacing, CFD Analysis, Absolute Pressure, Dynamic Pressure

1. Introduction

During long-term operation of the primary- and secondary-side piping systems of nuclear power plants, wall thinning, in which the pipe wall gradually becomes

thinner, may occur. Representative aging mechanisms responsible for pipe wall thinning include corrosion, FAC, and erosion. Because primary-side piping in nuclear power plants is primarily constructed of stainless steel, general corrosion or FAC relatively uncommon. In addition, because secondary-side systems are operated under strict water chemistry control, corrosion is generally not a significant concern. In contrast, erosion can cause localized damage to specific sections of piping through the physical interaction between the flowing fluid and the pipe wall, regardless of the pipe material or water chemistry conditions. Representative aging mechanisms observed in nuclear power plant piping include cavitation, flashing, liquid droplet impingement erosion (LDIE), and solid particle erosion (SPE) [1]. Unlike general corrosion and FAC, which typically affect relatively large surface areas, these erosion mechanisms can produce highly localized damage [2]. Because erosion results in localized wall thinning, the UT method commonly used for pipe wall thickness measurements may have limitations in accurately identifying erosion-damaged regions. Although EPRI NSAC-202L [3] provides recommended grid spacings for UT inspection, these recommendations were primarily developed for FAC, and guidance on appropriate grid spacing for detecting erosion damage remains limited.

Accordingly, this study presents the results of a CFD analysis conducted to determine the optimal inspection grid spacing for detecting erosion damage in piping, with a particular emphasis on cavitation, which is one of the most frequently observed erosion mechanisms in the primary- and secondary-side piping systems of nuclear power plants. A total of 22 CFD analyses were performed for four pipe sizes (2, 6, 10, and 12 inches), each equipped with an orifice plate. Five inlet pressure conditions were analyzed for the 2- and 6-inch pipes, while six conditions were considered for the 10-inch and 12-inch pipes. All simulations were performed using the commercial CFD software ANSYS FLUENT.

2. Mathematical Model and Numerical Methodology

2.1. Governing Equations

The multiphase flow was modeled using the Eulerian-based Mixture Model [4]. The mixture continuity and momentum equations were solved for the mixture phase, while the relative motion between the continuous and dispersed phases was accounted for through the drift-flux formulation. The mixture density and velocity were defined as the volume-weighted density and mass-averaged velocity, respectively.

$$\rho_m = \sum_k \alpha_k \rho_k \tag{1}$$

$$u_m = \frac{\sum_k \alpha_k \rho_k u_k}{\rho_m} \tag{2}$$

The mixture momentum equation was written as,

$$\frac{\partial(\rho_m u_m)}{\partial t} + \nabla \cdot (\rho_m u_m u_m) = -\nabla p + \nabla \tau_m + \rho_m g - \nabla \cdot \left(\sum_k \alpha_k \rho_k u_{dr,k} u_{dr,k} \right) \tag{3}$$

And the drift velocity is defined as follows.

$$u_{dr,k} = u_k - u_m \tag{4}$$

The Zwart-Gerber-Belamri (ZGB) cavitation model was also employed [5]. The ZGB model is based on the Rayleigh-Plesset equation and accounts for the growth and collapse of vapor bubbles, while the mass transfer associated with the phase change between the liquid and vapor phases is modeled through evaporation and condensation terms. Evaporation is assumed to occur when the local pressure is lower than the saturated vapor pressure, whereas condensation occurs when the local pressure is higher than the saturated vapor pressure. The transport equation for the vapor phase can be expressed as follows:

$$\frac{\partial(\rho_v \alpha_v)}{\partial t} + \nabla \cdot (\rho_v \alpha_v u_v) = \dot{m}_{evp} - \dot{m}_{cond} \tag{5}$$

Here, ρ_v, α_v and u_v denote the vapor-phase density, volume fraction, and velocity, respectively, while $\dot{m}_{evp}$ and $\dot{m}_{cond}$ represent the mass transfer rates due to evaporation and condensation, respectively. When the local pressure p is lower than the saturation vapor pressure p_v, the evaporation mass transfer rate is defined by Equation (6). Conversely, when the local pressure p is higher than the saturation vapor pressure p_v, the condensation mass transfer rate is defined by Equation (7).

$$\dot{m}_{evp} = F_{evap} \frac{3\alpha_{vc}(1-\alpha_v)\rho_v}{R_B} \sqrt{\frac{2}{3}\frac{p_v - p}{\rho_l}} \tag{6}$$

$$\dot{m}_{cond} = F_{cond} \frac{3\alpha_v \rho_v}{R_B} \sqrt{\frac{2}{3}\frac{p - p_v}{\rho_l}} \tag{7}$$

Here, R_B denotes the representative radius of the vapor bubbles, α_{vc} is the volume fraction of nucleation, F_{evap} and F_{cond} are the evaporation and condensation coefficients, respectively, and ρ_l and ρ_v represent the densities of the liquid and vapor phases, respectively. Accordingly, the ZGB model simulates the inception, growth, and collapse of cavitation by calculating the interphase mass transfer due to evaporation and condensation based on the difference between the local pressure in the flow field and the saturation vapor pressure.

2.2. Turbulence Model

For the analysis of pressure recovery and the recirculation region, the Transition SST k-ω model was employed as the turbulence model. The Transition SST model extends the conventional SST k-ω turbulence model by incorporating transport equations for the intermittency γ and the transition momentum-thickness Reynolds number $Re_{\theta,t}$ to simulate the laminar-transitional-turbulent transition process within the boundary layer [6]. The SST model uses turbulent kinetic energy k and specific dissipation rate ω as the primary turbulence variables, and its general form of the transport equations is expressed by Equations (8) and (9).

$$\frac{\partial(\rho k)}{\partial t}+\nabla\cdot(\rho uk)=P_k-\beta^*\rho k\omega+\nabla\cdot\left[(\mu+\sigma_k\mu_k)\nabla\mathrm{k}\right] \tag{8}$$

$$\frac{\partial(\rho\omega)}{\partial t}+\nabla\cdot(\rho u\omega)=\alpha\frac{\omega}{k}P_k-\beta^*\rho\omega^2+\nabla\cdot\left[(\mu+\sigma_\omega\mu_t)\nabla\omega\right]+CD_\omega \tag{9}$$

Here, P_k denotes the production term of turbulent kinetic energy, and the turbulent eddy viscosity is basically related as given in Equation (10).

$$\mu_t=\frac{\rho k}{\omega} \tag{10}$$

Descriptions of the remaining variables are omitted for brevity.

3. Computational Domain, Mesh, and Analysis Conditions

3.1. Analysis Model Configuration

Four pipes with Nominal Pipe Sizes (NPSs) 2, 6, 10 and 12 and Schedule 40, which are commonly used in nuclear power plants, were selected to determine the optimal inspection grid spacing for detecting erosion damage. The corresponding inner diameters are 52.48 mm (NPS 2), 154.08 mm (NPS 6), 254.51 mm (NPS 10), and 303.23 mm (NPS 12). For simplicity, the inner diameters were approximated as 50, 150, 250, and 300 mm, respectively. An orifice plate with a beta ratio ($\beta=d/D$) of 0.5 was adopted to induce cavitation. Figure 1 and Figure 2 illustrate the geometries of the NPS 2 and NPS 10 analysis models, respectively. To ensure fully developed downstream flow and sufficient recovery of the flow field after the orifice, the downstream sections of the NPS 10 and NPS 12 pipes were extended by an additional 300 mm compared with those of the NPS 2 and NPS 6 pipes. Five layers of boundary-layer meshes were generated adjacent to the pipe wall to accurately resolve the near-wall flow and turbulent viscosity effects.

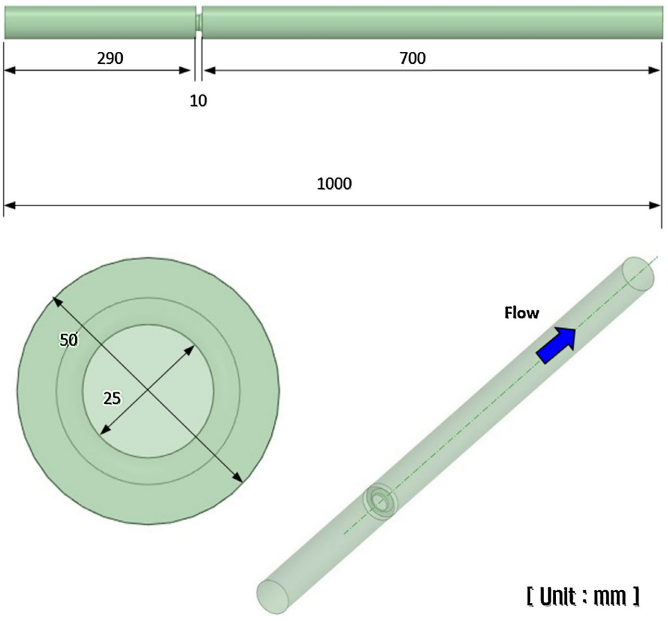


Figure 1. Analysis model for 2-inch pipe.

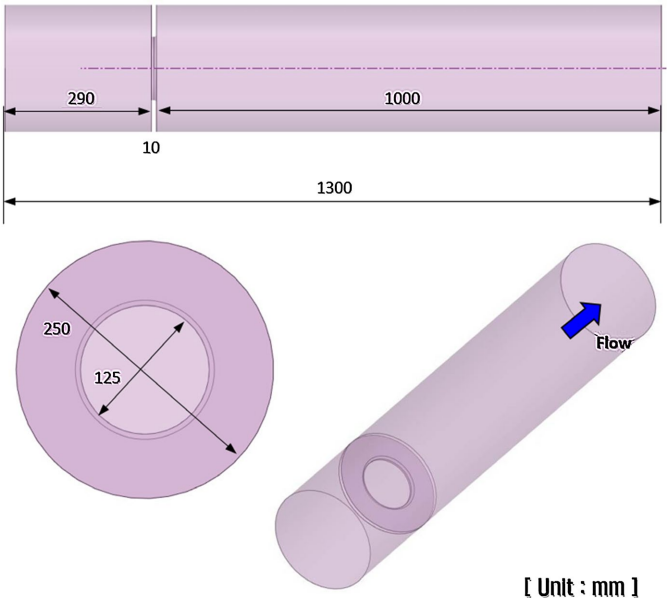


Figure 2. Analysis model for 10-inch pipe.

3.2. Mesh Independence Study

To ensure that the reported hydrodynamic results are free from numerical artifacts associated with spatial discretization, four mesh resolutions were tested for a 6-inch pipe at an inlet pressure of 90,000 Pa, with the total number of cells ranging from 77,397 to 696,444, as summarized in Table 1. The predicted liquid holdup at the end of the calculation increases monotonically with mesh refinement and asymptotically approaches the value obtained on the extra-fine mesh, with the deviation dropping from 8.08% (coarse mesh) to only 1.08% on the fine mesh. Accordingly, the mesh with 348,207 cells was selected for the 6-inch pipe simulation. For the remaining pipes, the number of cells was selected in proportion to the pipe diameter as shown in Table 2. Table 2 shows the mesh configuration and the number of cells of the analysis model. The total number of cells was determined in proportion to the inner diameter of each pipe.

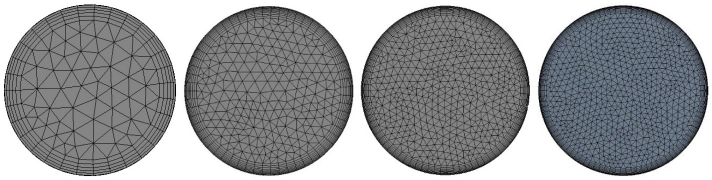
3.3. Analysis Conditions

Water at 90˚C was used as the working fluid for the CFD simulations of the four pipe sizes. The saturated vapor pressure (P_v) was set to 70,140 Pa. To investigate

Table 1. Results of mesh independence study.

Mesh Level	Number of Cells	Liquid Holdup (%)	Deviation from Finest Mesh (%)
Coarse	77,397	90.42	8.08
Medium	139,283	95.05	3.45
Fine	348,207	97.42	1.08
Extra Fine	696,444	98.50	0.0 (Reference)

Table 2. Number of cells and mesh style by nominal pipe size for analysis models.

NPS	2	6	10	12
Number of cells	151,842	348,207	552,054	688,322
Style				

cavitation behavior, the inlet pressure was varied, resulting in a total of 22 simulation cases: five inlet pressure conditions for the 2- and 6-inch pipes and six conditions for the 10- and 12-inch pipes. Multiple operating conditions were considered for each pipe size to investigate the occurrence of cavitation under various inlet pressures, improve the reliability of the results of the CFD analysis, and establish an appropriate inspection grid spacing. The outlet pressure was fixed at 0 Pa for all cases. The inlet pressure conditions used in the simulations are summarized in **Table 3**.

Table 3. CFD simulation cases.

Case	2-inch	6-inch	10-inch	12-inch
1	87,500	85,000	77,500	77,500
2	90,000	87,500	80,000	80,000
3	92,500	90,000	82,500	82,500
4	95,000	92,500	85,000	85,000
5	97,500	95,000	87,500	87,500
6	-	-	90,000	90,000

All simulations were performed under transient conditions for 3 s. To enhance numerical stability, the initial time step was set to 1×10^{-5} s, and the time step was maintained at no more than 1×10^{-3} s throughout the simulations. Gravitational effects were also included in all simulations.

4. Results of the CFD Analysis

Cavitation occurs when the local fluid pressure inside a pipe, such as in the region downstream of an orifice, falls below the saturated vapor pressure. The vapor cavities generated under these conditions collapse rapidly as the local pressure recovers above the saturated vapor pressure. The collapse of these cavities generates impact forces or pressure pulses that repeatedly act on the pipe wall, resulting in cavitation erosion. However, cavity collapse occurring sufficiently far from the pipe wall is expected to have little influence on erosion damage. Accordingly, CFD data were extracted at four sampling points located near the inner wall of the pipe, as illustrated in **Figure 3**. For each analysis model, four sampling lines were de-

fined along the pipe axis to evaluate the CFD results as a function of axial distance. As shown in Figure 3, the z-axis represents the axial direction of the pipe. The radial positions of each sampling points was set to 90% of the pipe radius measured from the pipe center, thereby locating the points outside the near-wall viscous sublayer.

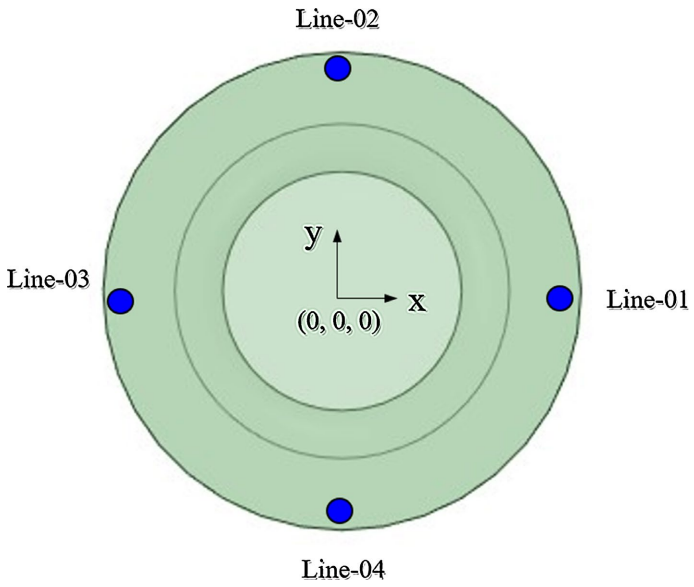
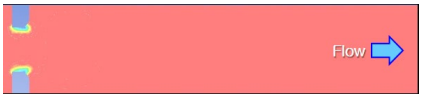
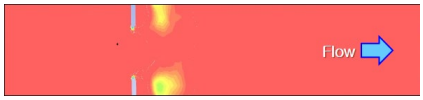
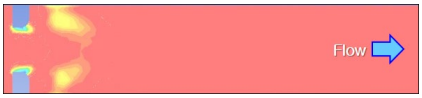
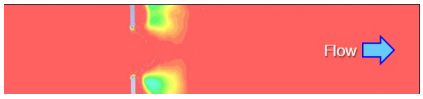
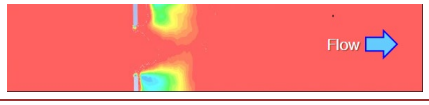


Figure 3. Data calculation points.

Table 4 presents the water volume fraction (WVF) distributions, illustrating the vapor formation patterns under different inlet pressure conditions for the 2-inch and 6-inch pipes. For both pipe sizes, the vapor volume fraction gradually

Table 4. WVF distributions at different inlet pressures for the 2- and 6-inch pipes.

Cases	2-inch		6-inch	
	Inlet Pressure, Pa	WVF	Inlet Pressure, Pa	WVF
1	87,500		85,000	
2	90,000		87,500	
3	92,500		90,000	
4	95,000		92,500	
5	97,500		95,000	

increases with increasing inlet pressure. A similar trend is observed for the 10-inch and 12-inch pipes.

The absolute pressure associated with vapor formation was compared with the flow variables obtained from the CFD simulations. In general, the highest vapor bubble density is observed in regions where the operating pressure recovers above the saturated vapor pressure after initially falling below it. The greatest number of collapsing vapor bubbles is also greatest in these regions.

Dynamic pressure, velocity magnitude, radial velocity, and shear stress were compared with the absolute pressure for all analyzed cases. Among these variables, dynamic pressure exhibited the strongest correlation with the location at which the pressure at the inner wall recovered above the saturated vapor pressure. Therefore, dynamic pressure was selected as the principal flow variable for determining the inspection grid spacing. Figure 4 and Figure 5 present sample comparisons between absolute pressure and dynamic pressure for the 2- and 6-inch pipes, respectively.

Figure 4 compares the absolute and dynamic pressures along Line-03 of the 2-inch pipe under an inlet pressure of 92,500 Pa. As indicated by the region enclosed by the red dashed line, the absolute pressure (blue circles) increases above the saturated vapor pressure (red solid line) during the initial pressure recovery stage, while the dynamic pressure (green diamonds) reaches its maximum value. Figure 5 presents the corresponding results for the 6-inch pipe along Line-03 under an inlet pressure of 87,500 Pa. In all cases, the dynamic pressure reaches its maximum in the vicinity of the location where the absolute pressure recovers above the saturated vapor pressure. Although dynamic pressure is not a direct indicator of vapor bubble collapse, it is an important flow parameter associated with static pressure recovery. According to Equation (11), vapor bubble collapse occurs as the static pressure increases and the dynamic pressure decreases, causing the

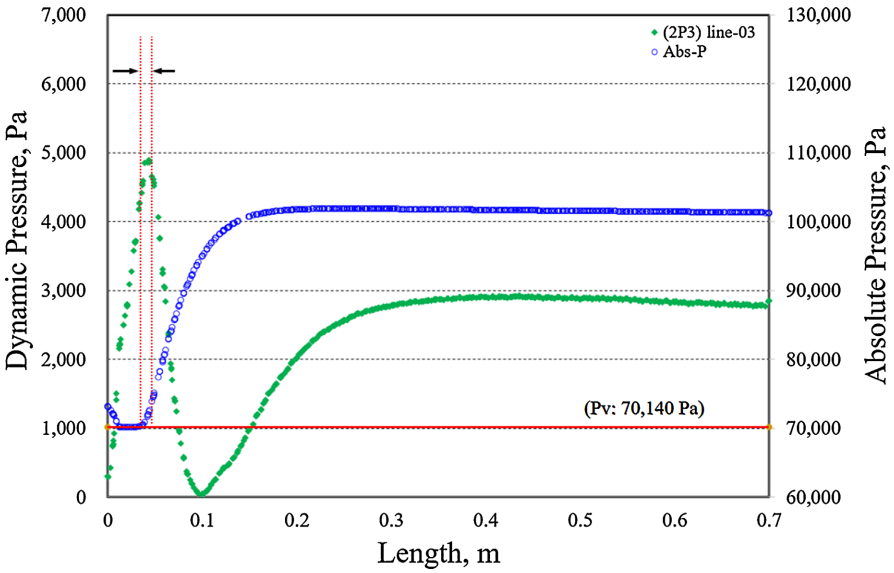


Figure 4. Comparison of absolute and dynamic pressures for 2-inch pipe.

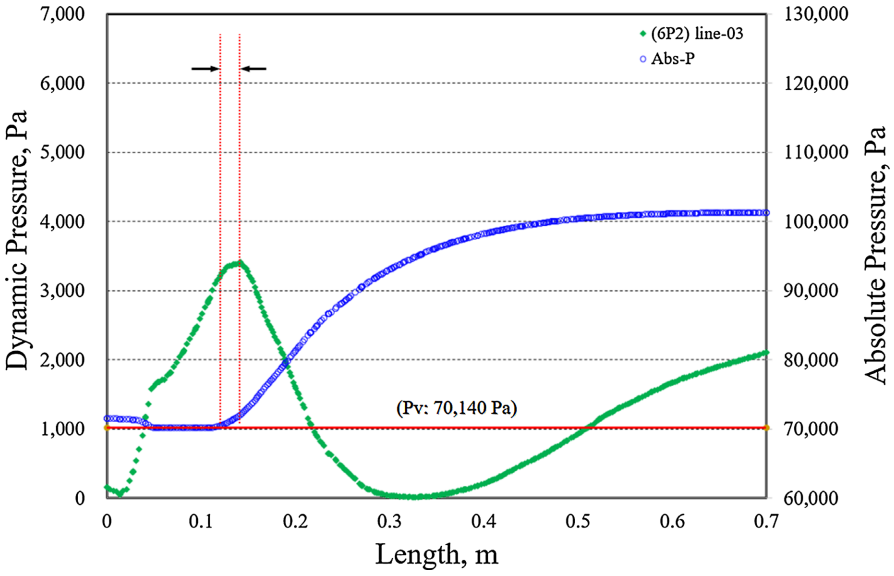


Figure 5. Comparison of absolute and dynamic pressures for 6-inch pipe.

absolute pressure to exceed the saturated vapor pressure. These observations indicate that dynamic pressure is closely associated with the occurrence of cavitation erosion on the inner surface of the pipe.

$$P_{static} + \frac{1}{2}\rho v^2 \approx \text{constant} \tag{11}$$

Accordingly, for each of the four pipe sizes, the axial distance corresponding to 90% of the maximum dynamic pressure was determined using the results obtained under five or six inlet pressure conditions. Figures 6-9 present comparisons of absolute pressure and dynamic pressure for the sampling lines exhibiting the highest calculated dynamic pressure for the 2-, 6-, 10-, and 12-inch pipes, respectively.

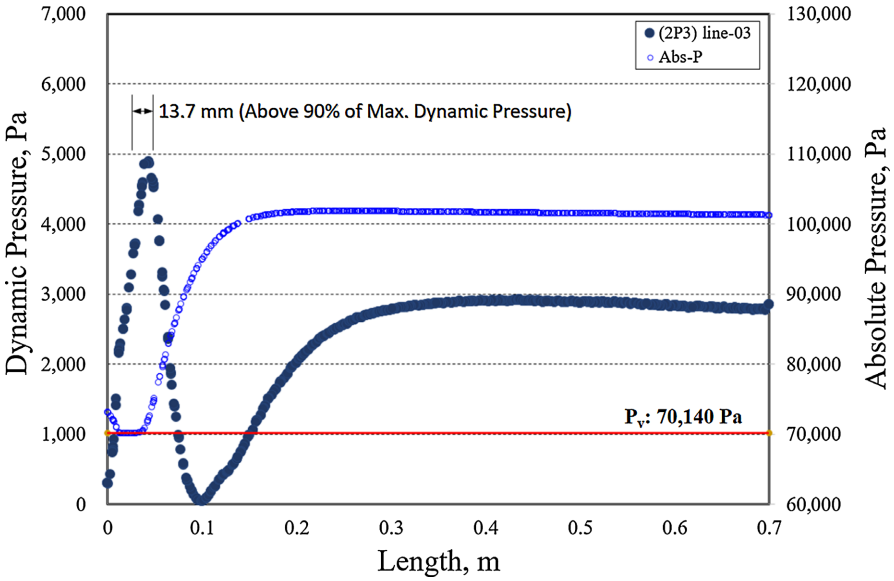


Figure 6. Distance corresponding to 90% of the maximum dynamic pressure for 2-inch pipe.

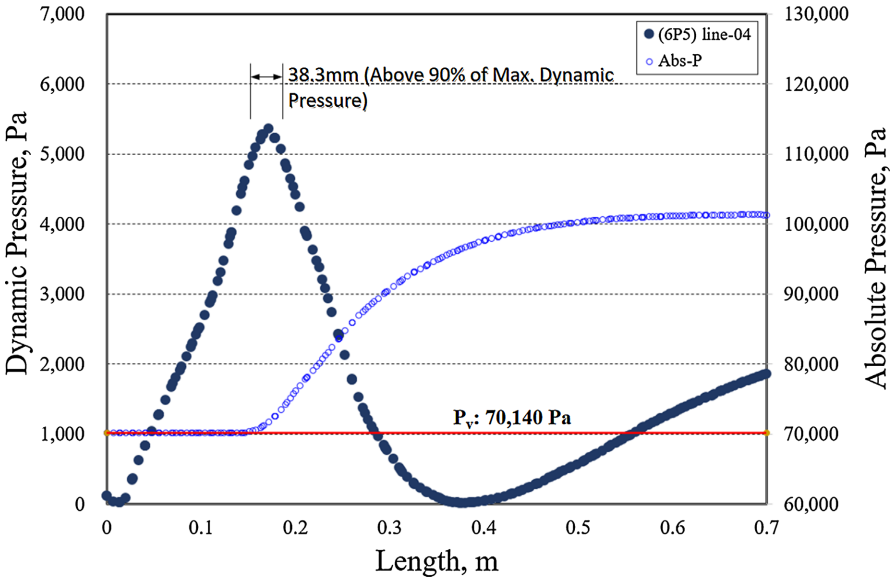


Figure 7. Distance corresponding to 90% of the maximum dynamic pressure for 6-inch pipe.

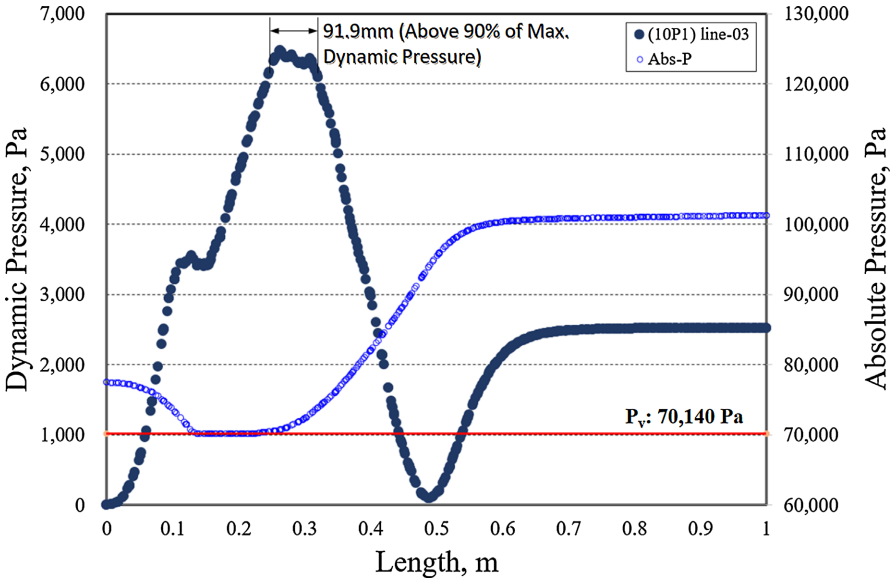


Figure 8. Distance corresponding to 90% of the maximum dynamic pressure for 10-inch pipe.

The axial distances at which the dynamic pressure reaches 90% of its maximum value are also indicated. The 90% criterion was adopted because, from the perspective of grid-based ultrasonic thickness (UT) inspection, at least one inspection point should be located within the region corresponding to 90% of the maximum dynamic pressure. Therefore, this distance was considered an appropriate basis for determining the UT inspection grid spacing.

5. Determination of the Inspection Grid Spacing

Table 5 and Figure 10 compare the inspection grid spacings recommended by

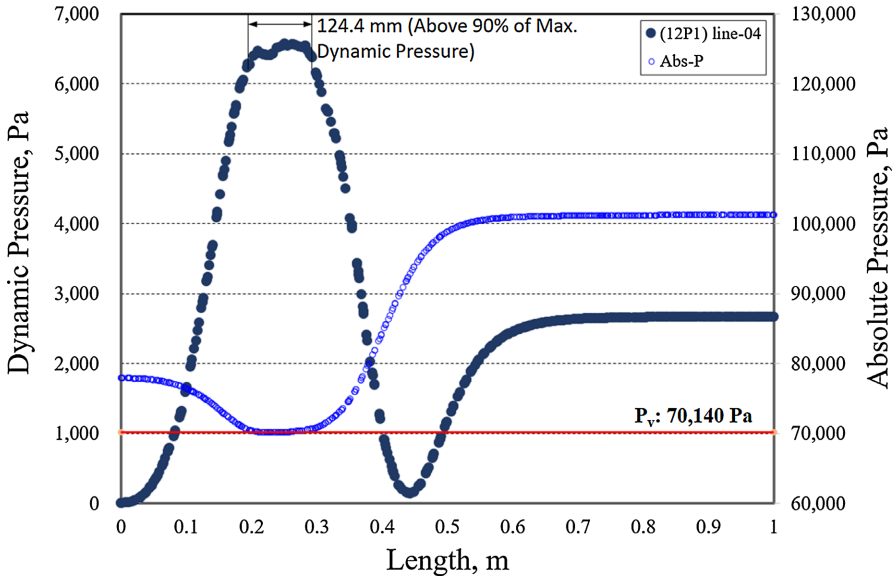


Figure 9. Distance corresponding to 90% of the maximum dynamic pressure for 12-inch pipe.

Table 5. Comparison of inspection grid spacing recommended by EPRI and those determined in CFD analysis.

NPS	Inspection grid spacings recommended by EPRI, mm	Inspection grid spacings derived from CFD analysis, mm	CFD/EPRI, %
2	25.4	13.7	53.9
6	44.0	38.3	87.1
10	71.0	91.9	129.5
12	85.0	124.4	146.3

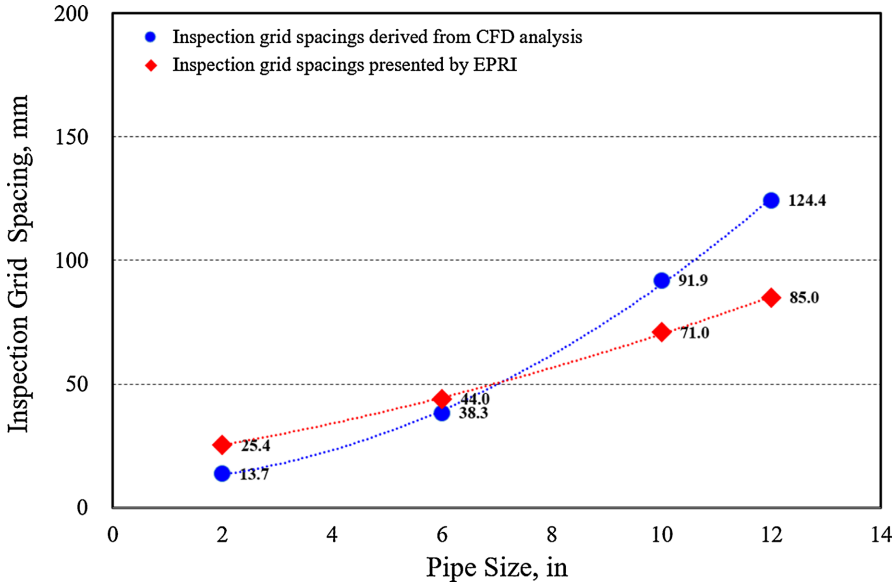


Figure 10. Comparison of inspection grid spacing recommended by EPRI and those determined in CFD analysis.

EPRI with those determined in the present study for the four pipe sizes. For the 2- and 6-inch pipes, the inspection grid spacings recommended by EPRI were greater than those determined in the present study. In contrast, for the 10- and 12-inch pipes, the grid spacings derived from the present CFD analysis were greater than the corresponding EPRI recommendations. The inspection grid spacings specified in EPRI NSAC-202L were adopted as the reference in this study because it is the only available guideline that provides quantitative recommendations for UT inspection grid spacing. However, these recommendations were originally developed for the inspection of FAC rather than cavitation erosion. Therefore, their direct application to cavitation erosion inspection may be limited.

For piping with a nominal diameter of 8 inches or greater, the inspection grid spacing recommended by EPRI appears to provide a sufficiently conservative basis for UT inspection of cavitation erosion. In contrast, for piping with a nominal diameter of less than 8 inches, the results of the CFD analysis suggest that reducing the inspection grid spacing to approximately one-half of the EPRI recommendation would improve the probability of detecting localized erosion damage. Nevertheless, reducing the inspection grid spacing inevitably increases the number of UT measurement points. Although a greater number of inspection points can improve the reliability of erosion detection, it also increases inspection time, labor requirements, and inspection costs. Therefore, an appropriate balance between inspection reliability and inspection efficiency should be considered when selecting the inspection grid spacing.

6. Conclusions

Ultrasonic testing is the most widely used method for inspecting pipe wall thinning. In grid-based UT inspection, a lattice grid is marked on the pipe surface, and wall thickness measurements are performed at the grid intersections. In the present study, the UT inspection grid spacings specified in EPRI NSAC-202L were adopted as the reference because they provide the only publicly available quantitative recommendations for UT inspection grid spacing. However, because these recommendations were originally developed for the FAC inspection, their direct application to cavitation erosion may be limited. Accordingly, cavitation simulations were performed for four pipe sizes equipped with orifice plates under a total of 22 operating conditions by varying the inlet pressure. To investigate the relationship between cavitation and erosion occurring on the inner surface of the pipe, the absolute pressure associated with vapor formation was compared with several CFD-derived flow variables. Among these variables, dynamic pressure exhibited the strongest correlation with the location at which the absolute pressure recovered above the saturated vapor pressure.

Based on these results, the axial distance corresponding to 90% of the maximum dynamic pressure was determined for all operating conditions. This region was considered the area most susceptible to cavitation erosion. Therefore, from the perspective of grid-based UT inspection, at least one inspection point should be

located within this region to improve the probability of detecting localized erosion damage.

Finally, the inspection grid spacings derived from the CFD analysis were compared with the recommendations provided in EPRI NSAC-202L. For piping with a nominal diameter of 8 inches or greater, the EPRI-recommended grid spacing appears to provide a sufficiently conservative basis for UT inspection. However, for piping with a nominal diameter of less than 8 inches, reducing the inspection grid spacing to approximately one-half of the EPRI recommendation is expected to improve the detection of localized cavitation erosion. Nevertheless, because reducing the inspection grid spacing inevitably increases the number of inspection points, inspection time, and inspection costs, an appropriate balance between inspection reliability and inspection efficiency should be considered when determining the inspection grid spacing.

Author Contributions

Conceptualization, Hwang, K. and Park, J.; methodology, Hwang, K.; software, Hwang, K.; validation, Kim, J. and Ko, B.; Kim, J. and Ko, B.; data curation, Hwang, K.; writing—original draft preparation, Hwang, K.; writing—review and editing, Kim, J. and Ko, B.; visualization, Hwang, K.; supervision, Hwang, K.; funding acquisition, Park, J. All authors have read and agreed to the published version of the manuscript.

Conflicts of Interest

The authors declare no conflicts of interest regarding the publication of this paper.

References

[1] Hwang, K., So, I. and Seo, H. (2022) Cause Analysis for Wall Thinning of Small-Bore Piping in Nuclear Power Plant by Tospace, FLUENT and Theoretical Evaluation. *World Journal of Nuclear Science and Technology*, **12**, 101-112. https://doi.org/10.4236/wjnst.2022.123009

[2] Crockett, H. and Findlan, S. (2007) Interim Recommendations for an Effective Program against Erosive Attack, EPRI Technical Update 1015071. Electric Power Research Institute, Palo Alto.

[3] Electric Power Research Institute (1999) Recommendations for an Effective Flow-Accelerated Corrosion Program. NSAC-202L-R2, Final Report, EPRI, Palo Alto.

[4] Dobran, F. (1992) Modeling of Structured Multiphase Mixtures. *International Journal of Engineering Science*, **30**, 1497-1505. https://doi.org/10.1016/0020-7225(92)90160-i

[5] Ezekoye, D., Zheng, Z. and Wu, J. (2024) Numerical Implementation and Verification of the Zwart-Gerber-Belamri Cavitation Model with the Consideration of Thermodynamic Effect. *Journal of Physics: Conference Series*, **2707**, Article ID: 012135. https://doi.org/10.1088/1742-6596/2707/1/012135

[6] Menter, F.R., Langtry, R. and Völker, S. (2006) Transition Modelling for General Purpose CFD Codes. *Flow, Turbulence and Combustion*, **77**, 277-303. https://doi.org/10.1007/s10494-006-9047-1